Journal of Materials Chemistry A

ROYAL SOCIETY OF CHEMISTRY

PAPER

View Article Online
View Journal | View Issue



Cite this: J. Mater. Chem. A, 2020, 8, 19879

# A universal pH range and a highly efficient $Mo_2C$-based electrocatalyst for the hydrogen evolution reaction†

Jiajia Huang,[a] Jingyi Wang,[a] Ruikuan Xie,[d] Zhihong Tian,*[c] Guoliang Chai,[d] Yanwu Zhang,[a] Feili Lai,[e] Guanjie He,*[bf] Chuntai Liu,[c] Tianxi Liu,[c] Paul R. Shearing[b] and Dan J. L. Brett[b]

Electrochemical water splitting is a promising approach to generate 'green' hydrogen. The efficiency of this process relies on the effectiveness of the electrocatalysts used. The electro-kinetics of the hydrogen evolution reaction (HER) is highly pH dependent and conventional catalysts typically are expensive and rare platinum-based materials. The development of low-cost, multi-component electrocatalysts, where each of the components has a synergistic effect, can be an effective approach to improve kinetics. Herein, a series of transition metal (Fe, Mn, Co, and Ni)-modified molybdenum carbides in a nitrogen-doped carbon matrix (TM-$Mo_2C$@NCF) are synthesised to maximise exposed active sites. Among them, Fe-$Mo_2C$@NCF delivers the best-in-class HER performance over a wide range of electrolytes. Tafel slopes of 76, 109 and 110 mV $dec^{-1}$ and overpotentials of 65, 130 and 129 mV at 10 mA $cm^{-2}$ were obtained in 1.0 M KOH, 1.0 M phosphate buffer solution (PBS) and 0.5 M $H_2SO_4$, respectively. The computational study further indicates that the synergistic electronic modulation co-activated by Fe and N dopants in Fe-$Mo_2C$@NCF can reduce the Gibbs free energy of H adsorption ($\Delta G_{H^*}$) and render the Mo–Mo bridge site the most energetically favorable adsorption site for the H* intermediate, which contributes to an increased HER performance.

Received 20th July 2020
Accepted 31st August 2020

DOI: 10.1039/d0ta07091b

rsc.li/materials-a



## 1. Introduction

Owing to its high energy density and ability to be generated from renewable sources of energy, hydrogen ($H_2$) is a promising alternative to fossil fuels to meet future global energy demands.[1–3] Electrochemical water splitting is considered to be one of the most effective means of 'green' hydrogen generation.[4–7] The production of hydrogen from water is a two-electron process, $2H^+ + 2e^- = H_2$, the electro-kinetics of which is highly pH dependent. Industrial production of hydrogen by water electrolysis can take place in acid or alkaline media, each having its relative merits and challenges, with the effect on the kinetics of the complementary oxygen evolution reaction (OER) playing an important role.[8,9] Ruthenium (Ru)-based materials for the OER and HER are very promising because of their prominent catalytic activity and universal pH application. Various modification strategies on Ru-based materials have been summarized and the general description about water splitting has been presented to understand the reaction mechanism, and key stability issues for Ru-based materials have been further investigated.[10,11] Additionally, it is desirable to achieve effective HER performance in neutral electrolytes for sea-water and microbial electrolysis.[12–14] Therefore, to meet practical requirements, an ideal HER electrocatalyst should operate effectively over the entire pH range. Pt-based materials are the benchmark for the HER in acid media owing to their low overpotential and suitable hydrogen adsorption Gibbs free energy; however, their cost and scarcity are a barrier to industrial use.[15,16] Therefore, extensive effort has been devoted to the development of hydrogen evolution catalysts based on noble-metal-free and earth-abundant resources.[17]

Mo-based catalysts are regarded as favorable candidates for the HER due to the modification of the d-band structure induced by the formation of a metal–carbon bond.[18,19] In the

[a]School of Chemical Engineering, Zhengzhou University, Zhengzhou 450001, P. R. China

[b]Electrochemical Innovation Lab, Department of Chemical Engineering, University College London, London WC1E 7JE, UK. E-mail: g.he@ucl.ac.uk

[c]Key Laboratory of Materials Processing and Mold (Zhengzhou University), Ministry of Education, National Engineering Research Center for Advanced Polymer Processing Technology, Zhengzhou University, Zhengzhou, Henan 450002, China. E-mail: zhihong.tian@zzu.edu.cn

[d]State Key Laboratory of Structural Chemistry, Fujian Institute of Research on the Structure of Matter, Chinese Academy of Sciences (CAS), Fuzhou, 350002 Fujian, P. R. China

[e]Department of Chemistry, KU Leuven, Celestijnenlaan 200F, Leuven 3001, Belgium

[f]School of Chemistry, University of Lincoln, Joseph Banks Laboratories, Green Lane, Lincoln, LN6 7DL, UK

† Electronic supplementary information (ESI) available. See DOI: 10.1039/d0ta07091b

past few decades, various Mo-based materials, such as molybdenum sulphides,[20–23] oxides,[24] nitrides,[25–27] phosphides,[28–30] and carbides,[31–33] have been emerging as prospective electrocatalysts for hydrogen production.[2,34,35] Representatively, molybdenum carbide ($Mo_2C$) has received wide attention and been intensively investigated as an HER catalyst on account of its abundance, low toxicity, similar Fermi level and d-electronic structure to Pt, and high resistance in various electrolytes.[36–38] Particularly, β-phase molybdenum carbide (β-$Mo_2C$) has demonstrated the highest activity among different crystalline phases of molybdenum carbides.[36] Previous research has shown that $Mo_2C$ has a relatively undesirable hydrogen binding energy ($\Delta G_{H^*}$) due to Mo atoms with a high density of an empty d-orbital; thus, it is easy to form strong Mo–H bonds on a $Mo_2C$ surface which is unfavorable for the desorption of active hydrogen, making the Heyrovsky/Tafel step partially restricted.[19,28,39,40] Many modification methods to optimize the activity of molybdenum carbide have been summarized; specific nanostructures and carbon-based hybrids are introduced to increase the active sites and promote mass transfer, and heteroatom doping is encouraged to improve the chemical configurations of active sites towards intrinsically boosted HER kinetics.[41,42] Elemental doping has been established to be a reliable method to regulate the electronic structure of materials.[43] Recently, the modification of $Mo_2C$-based materials, especially *via* introducing different elements into the $Mo_2C$ lattice, has been widely explored.[44,45] This method strongly affected their HER properties by regulating the electron density of such materials. Ma *et al.* reported porous molybdenum carbide (β-$Mo_2C$) spheres with novel surface engineered structures (coexistence of Co doping and Mo vacancies) to enhance the HER performance over the β-$Mo_2C$-based catalyst surface and tested their hydrogen evolution activity in acidic media.[46] Wan *et al.* reported a wide range of magnetic iron-doped molybdenum carbide ($Mo_{2-x}Fe_xC$) nanomaterials synthesised by the decomposition of a novel amine-metal oxide composite. They evaluated their hydrogen evolution activity in an acid environment, which required a ~300 mV overpotential to achieve a current density of 10 mA $cm^{-2}$.[47] Li *et al.* reported a two-dimensional coupled hybrid of molybdenum carbide and reduced graphene oxide with a ternary polyoxometalate-polypyrrole/reduced graphene oxide nanocomposite as a precursor and tested its hydrogen evolution activity in acidic media.[48] Xiong *et al.* reported Ni-doped $Mo_2C$ nanowires directly grown on Ni foam *via* a hydrothermal reaction combined with a carbonization process and tested their hydrogen evolution activity in alkaline media.[49] Furthermore, $Mo^{2+}$ sites have been proven to be important for promoting catalytic hydrogen evolution,[50,51] but their abundance among the $Mo_2C$ structures is difficult to control. Even though great effort has been made to the improvement of $Mo_2C$-based catalyst performance, tuning of properties for effective operation in neutral electrolytes, and further expanding the range of applications, is seldom achieved. Thus, a strategy to optimise the structure and electronic properties of $Mo_2C$-based materials is urgently required to implement these materials as an efficient noble metal-free 'pH-universal' HER catalyst.

Herein, we develop a facile annealing strategy to synthesise a series of transition metal (TM)-doped molybdenum carbide modified within porous nitrogen-doped carbon frameworks (TM-$Mo_2C$@NCF). Among them, iron-doped molybdenum carbide (Fe-$Mo_2C$) showing the most abundant $Mo^{2+}$ active species exhibits the highest catalytic HER activity and long-term stability for the HER under all media, thus making it easy to couple with any suitable OER catalysts in different electrolytes. This is ascribed to the merits of high intrinsic activity from the combination of $Fe^{2+}$ and $Mo^{2+}$ in $Mo_2C$, which exposes more Mo–Mo bridge active sites, as well as the stabilising effect of the nitrogen-doped carbon frameworks. Density functional theory (DFT) calculations are also applied to elucidate the underlying mechanism behind the distinct performance by comparing the electronic structure, hydrogen chemisorption process and Gibbs free energy of pure $Mo_2C$ and Fe-$Mo_2C$@NCF.

## 2. Experimental

### 2.1 Synthesis of TM-$Mo_2C$@NCF

The preparation of the various TM-$Mo_2C$@NCF materials all followed a similar procedure. The amount of $C_2H_2O_4 \cdot 2H_2O$ and melamine remained unchanged with a molar ratio of 2 : 1. Typically, Fe-$Mo_2C$@NCF was synthesised as follows. Firstly, 2.48 g (2 mmol) of $(NH_4)_6Mo_7O_{24} \cdot 4H_2O$ and 2.52 g (0.02 mol) of $C_2H_2O_4 \cdot 2H_2O$ were dissolved in 40 mL of deionized water. 1.26 g (0.01 mol) of melamine was added to the above clear solution, and then the mixture was kept at 70 °C for 6 h under magnetic stirring. Then, 5 mL of $Fe_2(SO_4)_3$ solution (0.07 mmol of $Fe^{3+}$) was added into the above mixed solution, stirring at 70 °C for 12 h progressively. After filtration, the precipitate was washed with deionized water and ethanol, then dried under vacuum at 60 °C. During this process, a composite containing Fe salts, oxalate and molybdate was formed, which was used as the precursor. Subsequently, the precursor was calcined at 800 °C for 3 h with a heating rate of 5 °C $min^{-1}$ under a continuous $N_2$ flow. To investigate the effects of different doped metals (Mn/Fe/Co/Ni) on the hydrogen evolution performance, Mn/Co/Ni-doped materials were prepared according to Table S1 in the ESI.† The obtained products were denoted as sample xTM-$Mo_2C$@NCF, where $x$ is the molar ratio of TM : Mo, respectively.

### 2.2 Electrocatalytic HER

The electrochemical measurements are carried out at room temperature using a CHI 660E potentiostat. Ag/AgCl (3 M KCl) and a graphite rod are used as a reference electrode (RE) and a counter electrode (CE) respectively. According to the formula $E$ (RHE) = $E$ (Ag/AgCl) + 0.0591 × pH + 0.2 V, all potentials can be converted to the reversible hydrogen electrode (RHE). The catalyst ink can be prepared by mixing a solution containing 190 μL of distilled water, 50 μL of ethanol, 5 wt% Nafion solution (10 μL) and the catalyst (2.0 mg) after an hour of sonication in an ice water bath. Thereafter, the surface of carbon paper (coated area: 0.5 × 1 $cm^2$) is loaded with 100 μL of the prepared catalyst ink, wherein 1.6 mg $cm^{-2}$ is calculated to be the loading

 

amount. To compare the properties of the as-prepared catalysts, linear sweep voltammetry (LSV) is conducted at a scan rate of 5 mV $s^{-1}$. A commercial 20 wt% Pt/C catalyst is used as the reference material for comparison of performance. The polarization curves were plotted as overpotential ($\eta$) *versus* log current ($\log j$) to get Tafel plots for evaluating the HER kinetics. The Tafel slope ($b$) as an intrinsic property of the catalyst was obtained by fitting the linear portion of Tafel plots according to the Tafel equation ($\eta = b\log(j) + a$) that can describe the rate-determining step of the HER process. Regarding the evaluation of the electrochemically active surface areas (ECSAs) of the catalysts, CV tests were performed by measuring the electrical double-layer capacitances ($C_{dl}$) with different scan rates (10, 20, 30, 40, 50, 60, 70, 80, 90 and 100 mV $s^{-1}$). The chronoamperometry measurements of 0.5% Fe-$Mo_2C$@NCF are conducted at an overpotential of 105 mV and negligible degradation can be observed after a 12 h process. In addition, after continuous CV scans at a scan rate of 100 mV $s^{-1}$, the overpotential differences of the polarization curves before and after the 1000 CV cycles between −0.1 and 0.1 V (*vs.* Ag/AgCl) were compared. Note that all the as-measured current densities were corrected to reduce the effect of ohmic resistance.

### 2.3 Characterization

XRD patterns were recorded using a Bruker D8 Advance X-ray diffractometer with a Cu Kα source. The $2\theta$ angular region of the XRD pattern between 20° and 80° was studied at a scan rate of 0.1 $s^{-1}$ with each step of 0.02°. The microstructures and compositions of samples were analyzed using scanning electron microscopy (SEM, Zeiss/Auriga Focused ion beam SEM), transmission electron microscopy and high-resolution transmission electron microscopy (TEM and HRTEM, FEI TalosF200S). X-ray photoelectron spectroscopy (XPS) measurements were performed on an ESCALAB 250 instrument (Thermo Electron) with Al Kα radiation. Raman spectra were collected using a LabRAM HR Evolution Laser Raman Spectrometer with a 532 nm laser diode as the excitation source. Brunauer–Emmett–Teller (BET) surface area measurements were obtained using a Micromeritics ASAP2460 with nitrogen adsorption at 77k. The amount of doped metal (Mn, Fe, Co, and Ni) in the samples was determined by ICPAES (ICPE-9820, SHIMADZU).

## 3. Results and discussion

Fe-$Mo_2C$@NCF nanostructures were synthesised by the solid-state thermolysis of a melamine-related composite of oxalate, Mo sources and Fe precursors. As for a typical synthesis, 0.5% Fe-$Mo_2C$@NCF was produced from annealing the precursor containing Fe salts, oxalate and molybdate. The crystalline phases of $x$Fe-$Mo_2C$@NCF characterised *via* XRD are shown in Fig. 1a, and the XRD patterns of $x$M-$Mo_2C$-@NCF (M = Mn/Co/Ni) are shown in Fig. S1.† The peaks located at $2\theta$ of 34.4°, 37.9°, 39.4°, 52.1°, 61.5°, 69.6°, 72.4° and 74.6° are assigned to (100), (002), (101), (102), (110), (103), (200) and (112) planes of the hexagonal β-$Mo_2C$ (PDF no. #35-0787); the phase is consistent with other reported electrocatalysts that presented the highest HER

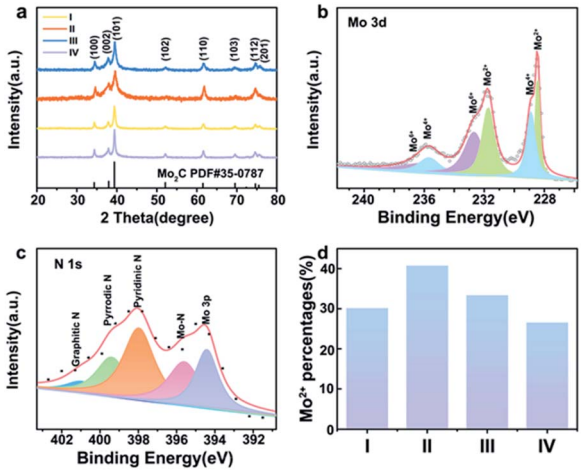


Fig. 1 Powder XRD patterns of Fe-doped materials, in which I/II/III/IV represent 0.2% Fe-$Mo_2C$@NCF, 0.5% Fe-$Mo_2C$@NCF, 1% Fe-$Mo_2C$@NCF and undoped $Mo_2C$@NCF, respectively. XPS spectrum of (a) Mo 3d (b)and N 1s (c) in 0.5% Fe-$Mo_2C$@NCF, and its surface $Mo^{2+}$ percentages (d) compared with other materials, in which I/II/III/IV represent 0.2% Fe-$Mo_2C$@NCF, 0.5% Fe-$Mo_2C$@NCF, 1% Fe-$Mo_2C$@NCF and undoped $Mo_2C$, respectively.

activities;[52–54] similar distribution of peaks indicates that they are all β-$Mo_2C$ phase.[55] No other diffraction peaks of impurities were detected and the as-prepared catalysts all display a high crystallinity. However, the patterns of β-$Mo_2C$ in the 0.5% Fe-$Mo_2C$@NCF catalyst shows a slight shift to a higher diffraction region, in comparison with pure $Mo_2C$ (Fig. S2, ESI†). This shift of the diffraction peaks is attributed to the shrinkage of the $Mo_2C$ unit cell because the radius of iron is smaller than that of molybdenum. The absolute values of lattice parameters and unit cell volumes for undoped and Fe modified samples are listed in Table S2.† Both lattice parameters ($a$/$b$ and $c$) and unit cell volume follow similar trends, decreasing with the increase of Fe doping amount from 0 to 0.31%, and the replacement of some Mo atoms with smaller Fe in the lattice contributes to the shrinking of the $Mo_2C$ unit cell. The Mn/Fe/Co/Ni doping amount of all the as-prepared catalysts is determined by inductively coupled plasma atomic emission spectroscopy (ICPAES) (Table S3, ESI†). Moreover, the BET surface area of 0.5% Fe-$Mo_2C$@NCF (29.5 $m^2$ $g^{-1}$) is higher than that of undoped $Mo_2C$ (23.9 $m^2$ $g^{-1}$), which could increase the active sites.

To identify the chemical environment of $x$Fe-$Mo_2C$@NCF on the surface, XPS analysis was conducted. Fig. S3† shows the full XPS profiles of 0.5% Mn-$Mo_2C$@NCF, 0.5% Fe-$Mo_2C$@NCF, 0.5% Co-$Mo_2C$@NCF and 0.5% Ni-$Mo_2C$@NCF. From the XPS survey analysis shown in Fig. S3b,† the surface of 0.5% Fe-$Mo_2C$@NCF is composed of Mo, N, C and O. There is no obvious Fe peak because the doping content of Fe is relatively low. The peak fitting of Mo 3d verifies the existence of $Mo_2C$ ($Mo^{2+}$ at 228.5 and 231.7 eV). Moreover, $Mo^{4+}$ at 228.9 and 235.6 eV and $Mo^{6+}$ at 232.7 and 236.1 eV originate from surface oxidation (Fig. 1b). The presence of higher oxidation states from XPS is acceptable owing to the unavoidable surface oxidation layers of carbide materials, particularly for the nanosized ones, which

are easily oxidized on the surface.[56] Similarly, Mo 3d spectra of 0.5% Mn-$Mo_2C$@NCF, 0.5% Co-$Mo_2C$@NCF and 0.5% Ni-$Mo_2C$@NCF are displayed in Fig. S4.† As can be seen from Fig. 1c, the N 1s XPS spectrum is deconvoluted into five peaks at 394.57, 396.21, 398.23, 399.84 and 401.49 eV, which correspond to Mo 3p, Mo–N, pyridinic-N, pyrrolic-N, and graphitic-N, respectively, implying N-doping in the carbon matrix and the joint binding of Mo with the carbon skeleton.[35,57,58] In particular, pyridinic-N exhibits the highest peak from the spectrum and it was verified as advantageous for enhancing the catalytic performance of water splitting.[59] The increase of the $Mo^{2+}$ content should be attributed to the addition of transition metals, which is proved to be beneficial for the HER.[60] By comparing the peak area of $Mo^{2+}$ in materials with different molar ratios of Fe/Mo (Fig. 1d) and different types of TM doping (Fig. S4d, ESI†), it is obvious that $Mo^{2+}$ species are the most abundant when the molar ratio of Fe to Mo is 0.5 : 100, according to the XPS analysis, which indicates that doped iron is combined tightly with Mo atoms that leads to an increase of the $Mo^{2+}$ content in the molybdenum carbide catalysts. The increased $Mo^{2+}$ species further enrich the active sites on the surface of the materials, and also improve the electron density, which has a positive effect on the hydrogen evolution catalytic properties.

Fig. S5 and S6† show scanning electron microscope (SEM) and TEM images of 0.5% Mn-$Mo_2C$@NCF, 0.5% Fe-$Mo_2C$@NCF, 0.5% Co-$Mo_2C$@NCF and 0.5% Ni-$Mo_2C$@NCF, respectively. It can be seen that the morphology of these materials has negligible differences because all materials were synthesised under the same conditions, except using different TM precursors. In particular, 0.5% Fe-$Mo_2C$@NCF has a rougher surface, which consists of nanoparticles with several pits and is beneficial to exposing more active species. TEM images of both pure β-$Mo_2C$ (Fig. 2a) and 0.5% Fe-$Mo_2C$@NCF (Fig. 2d) show the analogous nanoparticle shape with the particle size of about 15 nm. The *d*-spacing (2.3 Å, Fig. 2b) and SAED (Fig. 2c) pattern are consistent with the (101) plane of β-$Mo_2C$. In Fig. 2e, β-$Mo_2C$ nanoparticles are wrapped by amorphous carbon. The existence of graphitic carbon has also been confirmed by the XRD patterns in Fig. 1a. The presence of a graphitic carbon support is another crucial factor to improve catalytic properties for the entire system.[60–62] Raman spectroscopy was performed to reveal the carbon structure of the catalysts by the ratio of $I_D/I_G$. The Raman spectra (Fig. S6, ESI†) exhibit double peaks at around 1347 $cm^{-1}$ and 1593 $cm^{-1}$, where the D-band (1347 $cm^{-1}$) was associated with $sp^2$ nanocrystalline carbon while the G-band (1593 $cm^{-1}$) corresponded to $sp^2$ amorphous carbon materials, the large $I_D/I_G$ implying that more defects formed on the NCF, thus favoring the accessibility of more active sites and enhancing the catalytic properties. EDS mapping *via* HRTEM in Fig. 2g–i proves that Mo, Fe and N are uniformly distributed and overlapped in the particles.

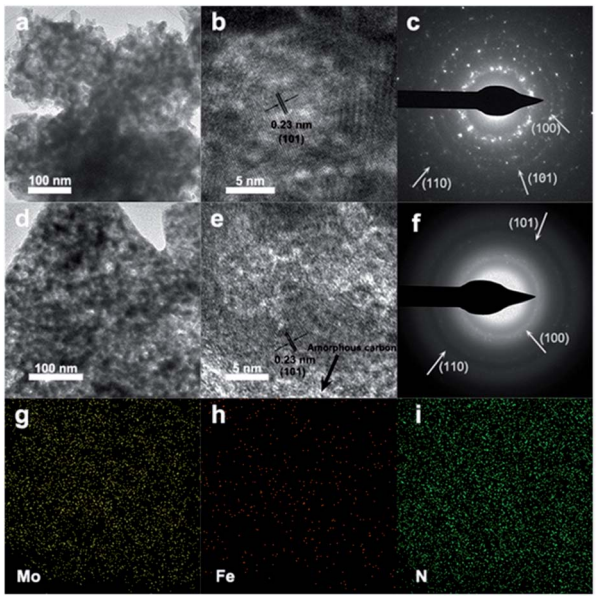


Fig. 2 (a) TEM image, (b) HRTEM image, and (c) SAED pattern of pure β-$Mo_2C$. (d) TEM image, (e) HRTEM image, and (f) SAED pattern of 0.5% Fe-$Mo_2C$@NCF. The corresponding EDS mapping images of (g) Mo, (h) Fe and (i) N for 0.5% Fe-$Mo_2C$@NCF.

As for the development of electrocatalytic technology, catalysts that are only suitable for acidic environments limit the range of practical applicability.[63–66] For example, microbial electrolysis and alkaline electrolysis need catalysts to be efficient in neutral and alkaline media, respectively.[64,65] Therefore, more electrocatalysts with high activity and stability in alkaline or neutral media need to be developed.[67] To get a more comprehensive evaluation of the electrocatalytic HER activity, the performance was measured in alkaline solution (1.0 M KOH, pH = 13.9), 1.0 M phosphate buffer solution (pH = 7) and acid solution (0.5 M $H_2SO_4$, pH = 0.1) with a fixed mass loading of 1.6 mg $cm^{-2}$ on the carbon paper. For a comparative study, Pt/C (20 wt%) was also examined for HER activity.

To obtain further insight into the HER activities of the electrocatalysts, the kinetic parameters evaluating the performance are summarised in Table S2 and Fig. S7.† The electrocatalytic activity of the materials was primarily investigated in alkaline media. In alkaline electrolyte, the 0.5% Fe-$Mo_2C$@NCF afforded a relatively low $\eta$ of 65 mV to reach the current density of 10 mA $cm^{-2}$ and 172 mV for 100 mA $cm^{-2}$ (Fig. 3a), which is 16 and 244 mV less than that for undoped $Mo_2C$, respectively. For highly active catalysts, the cathode current rises rapidly when a more negative potential is applied. Comparatively, 0.2% Fe-$Mo_2C$@NCF, 1% Fe-$Mo_2C$@NCF and undoped $Mo_2C$ show higher overpotentials of 199, 235 and 416 mV at a current density of 100 mA $cm^{-2}$, respectively; indicating that 0.5% Fe-$Mo_2C$@NCF exhibits the highest activity in alkaline environments. Consistent with the XPS results, the 0.5% Fe doping content results in the most abundant $Mo^{2+}$ species on the surface of $Mo_2C$, which exposes more active sites, and reaches the peak of the Fe–N–Mo cooperative coordination and shows the best HER activity.[68] For the integral HER process, the reaction step is the combination of the Volmer reaction and the Heyrovsky or Tafel reaction to generate $H_2$, and generally referred to as the Volmer–Heyrovsky or Volmer–Tafel process. By plotting overpotential ($\eta$) against log current (log *J*), the Tafel slope was obtained and kinetic parameters for the HER were calculated. The linear part of the Tafel plots (Fig. 3b) reveals

 

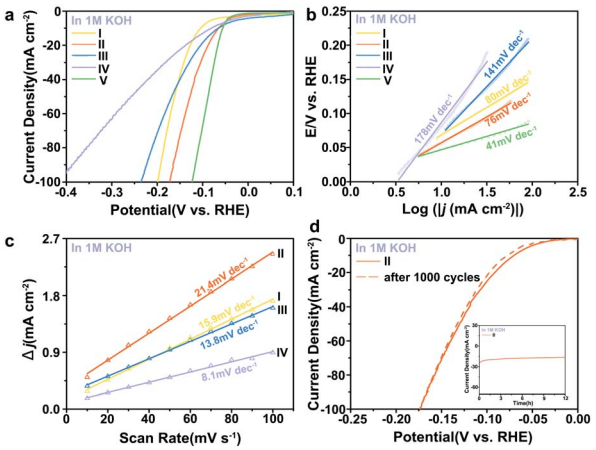


Fig. 3 (a) The iR-corrected polarization curves at a scan rate of 5 mV $s^{-1}$ and (b) the Tafel slopes of (I) 0.2% Fe-$Mo_2C$@NCF, (II) 0.5% Fe-$Mo_2C$@NCF, (III) 1% Fe-$Mo_2C$@NCF, (IV) undoped $Mo_2C$, and (V) Pt/C (20%) electrocatalyst in 1.0 M KOH. (c) Estimation of $C_{dl}$ through plotting the difference of current densities against the scan rates to fit a linear regression of I, II, III and IV. (d) Polarization curves of 0.5% Fe-$Mo_2C$@NCF (II) before and after 1000 cycles. Chronoamperometry curves at $\eta = -105$ mV (*vs.* RHE) shown in the inset (in 1.0 M KOH).

Tafel slopes of ~80, ~76, ~141 and ~178 mV $dec^{-1}$ for 0.2% Fe-$Mo_2C$@NCF, 0.5% Fe-$Mo_2C$@NCF, 1% Fe-$Mo_2C$@NCF and undoped $Mo_2C$, respectively. This illustrates that hydrogen evolution on 0.5% Fe-$Mo_2C$@NCF proceeds *via* the Volmer–Heyrovsky mechanism and that the electrochemical desorption step is rate-limiting. Compared with other electrocatalysts, except Pt/C, the exchange current density of 0.5% Fe-$Mo_2C$@NCF is the highest (~1.02 mA $cm^{-2}$). It is logical to ascribe the increased activity to the larger electrochemically active surface area (ECSA). One method to estimate the ECSA is to measure the double-layer capacitance ($C_{dl}$).[69,70] Based on the cyclic voltammograms (CVs) at different scan rates (Fig. S8, ESI†) in the region of +0.81 and +0.86 V (*vs.* Ag/AgCl), where the current response is due to the charging of the double-layer capacitance (non-faradaic current region), the capacitances of 0.2% Fe-$Mo_2C$@NCF, 0.5% Fe-$Mo_2C$@NCF, 1% Fe-$Mo_2C$@NCF and undoped $Mo_2C$ are calculated to be 15.9, 21.4, 13.8 and 8.1 mF $cm^{-2}$, respectively. This reveals the highest ECSA, and consequently the greatest number of catalytic active sites, for 0.5% Fe-$Mo_2C$@NCF (Fig. 3c). As a potentially effective candidate for the HER, the stability of a catalyst is also a key index. The durability of the 0.5% Fe-$Mo_2C$@NCF electrode was tested by conducting continuous cyclic voltammetry (CV) scanning between −0.1 V and 0 V *vs.* RHE at a scan rate of 10 mV $s^{-1}$ in 1.0 M KOH. After 1000 cycles, the 0.5% Fe-$Mo_2C$@NCF still performs efficiently with negligible loss of cathodic current density (Fig. 3d). Moreover, the chronoamperometric test of this electrode by electrolysis at a fixed overpotential of 105 mV also suggests its good durability (Fig. 3d).

It is of importance to mention that the 0.5% Fe-$Mo_2C$@NCF electrode also performs well in 1.0 M PBS for the HER. It is clear that pure $Mo_2C$ has poor catalytic activity towards the HER. The polarization curves of 0.5% Fe-$Mo_2C$@NCF in 1.0 M PBS are shown in Fig. 4a, which demonstrate an overpotential of 130 mV *vs.* RHE to reach a current density of 10 mA $cm^{-2}$ and relatively low overpotential of 275 mV to reach 100 mA $cm^{-2}$. In contrast, 0.2% Fe-$Mo_2C$@NCF, 1% Fe-$Mo_2C$@NCF and undoped $Mo_2C$, showed higher overpotentials of 406, 378 and 484 mV, respectively, at a current density of 100 mA $cm^{-2}$ in buffer solution. Fig. 4b shows the Tafel plots of 0.2% Fe-$Mo_2C$@NCF, 0.5% Fe-$Mo_2C$@NCF, 1% Fe-$Mo_2C$@NCF and undoped $Mo_2C$, which are consistent with LSV test results that 0.5% Fe-$Mo_2C$@NCF provided the smallest Tafel slope (109 mV $dec^{-1}$) compared to other electrodes. It is noted that the 0.5% Fe-$Mo_2C$@NCF electrode maintains long-term durability for the HER in 1.0 M PBS (Fig. 4g); the polarization curves of 0.5% Fe-$Mo_2C$@NCF exhibit a subtle decay after 1000 cycles of continuous cyclic voltammograms, illustrating the stability of the prepared catalysts and the resistance to accelerated degradation. The HER performances for the above catalysts were also tested in 0.5 M $H_2SO_4$. For 0.5% Fe-$Mo_2C$@NCF, it requires an overpotential of 129 mV to drive 10 mA $cm^{-2}$ and 242 mV for 100 mA $cm^{-2}$ (Fig. 4d), which is much smaller than that of undoped $Mo_2C$ at 10 mA $cm^{-2}$ (162 mV). 0.5% Fe-$Mo_2C$@NCF shows a lower Tafel slope (110 mV $dec^{-1}$) than pure $Mo_2C$ (131 mV $dec^{-1}$), as shown in Fig. 4e. Its stability in acid media was also evaluated. As observed, there is negligible loss in current density after 1000 continuous CV cycles (Fig. 4h), and its activity can be maintained for at least 12 h in both neutral and acidic media (Fig. 4i).

The hydrogen evolution properties of three groups of materials doped with manganese, cobalt, and nickel atoms in different proportions were also tested in acidic, neutral, and alkaline media (Fig. S9–S11 and Tables S6–S8, ESI†). Comparing the performance of the most active materials in the other three groups (0.5% Mn-$Mo_2C$@NCF, 0.5% Co-$Mo_2C$@NCF, and 0.5%

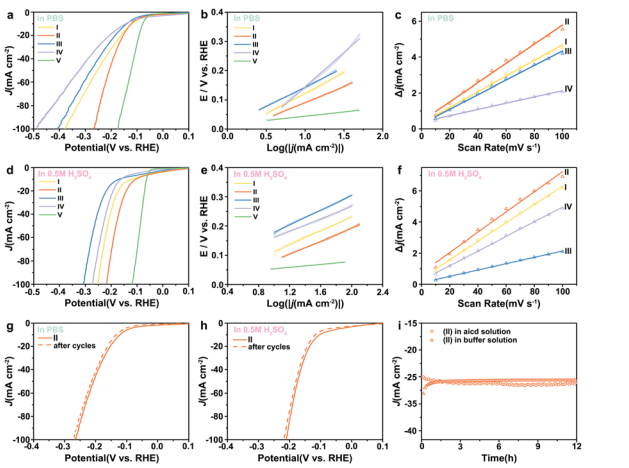


Fig. 4 The iR-corrected polarization curves at a scan rate of 5 mV $s^{-1}$ and the corresponding Tafel slopes of (I) 0.2% Fe-$Mo_2C$@NCF, (II) 0.5% Fe-$Mo_2C$@NCF, (III) 1% Fe-$Mo_2C$@NCF, (IV) undoped $Mo_2C$, and (V) Pt/C (20%) electrocatalysts in 1.0 M PBS (a and b) and in 0.5 M $H_2SO_4$(d and e); $C_{dl}$ of I, II, III and IV in 1.0 M PBS (c) and in 0.5 M $H_2SO_4$ (f); polarization curves of 0.5% Fe-$Mo_2C$@NCF before and after 1000 cycles in 1.0 M PBS (g) and 0.5 M $H_2SO_4$ (h); chronoamperometry curves at $\eta = -160$ mV (*vs.* RHE) in 1.0 M PBS and 0.5 M $H_2SO_4$ (i).

Ni-$Mo_2C$@NCF) with 0.5% Fe-$Mo_2C$@NCF, as shown in Fig. 5, it can be seen that the performance of 0.5% Fe-$Mo_2C$@NCF in three different pH media is still the best and attributed to the more abundant $Mo^{2+}$ active sites. As further compared with the current noble-metal-free catalysts (Tables S9 and S10, ESI†), the 0.5% Fe-$Mo_2C$@NCF material shows the best-in-class performance.

To gain further insight into the high electrocatalytic activity of the 0.5% Fe-$Mo_2C$@NCF electrocatalyst, DFT calculations were performed by constructing correlative theoretical models (Fig. S12–S19†). The adsorption free energy of H ($\Delta G_{H^*}$) can serve as an accepted measure for the activity of a catalytic material for the HER, for which a catalyst that gives $\Delta G_{H^*}$ close to 0 is considered a good candidate for the HER. The calculations of $\Delta G_{H^*}$ for 0.5% Fe-$Mo_2C$@NCF are described in Fig. 6. For comparison, a similar calculation was performed on pristine $Mo_2C$ and 1% Fe-$Mo_2C$@NCF. The influence of Fe dopants is investigated by replacing Mo atoms by Fe atoms. Four different doping sites for single Fe dopants are considered (Fig. S13†) to simulate the 0.5% Fe-$Mo_2C$@NCF material. The structure with the lowest formation energy is used for the following HER study (Fig. S13d and S14†). Eight different initial H* adsorption sites are considered and five different adsorption models were obtained after relaxation, as shown in Fig. S15.† The site with the strongest binding between H* is shown in Fig. S15c and S16.† The limiting potential of the HER on 0.5% Fe-$Mo_2C$@NCF is 0.39 V (Fig. 6a), which shows a better HER catalytic activity than pristine $Mo_2C$, and the HER catalytic activity decreases with a higher Fe concentration (two Fe dopants, 0.46 V). This is in agreement with the experimental results discussed above. In fact, the Mo–Mo bridge site in Fig. S13d† was found to be the most energetically favorable adsorption site for the H* intermediate in 0.5% Fe-$Mo_2C$@NCF (shown in the ESI†). To reveal the mechanism of how Fe dopants enhance the HER activity on $Mo_2C$, the electronic properties of the atoms on the adsorption sites have been studied. As shown in Fig. 6b, the d-band center of Mo in pristine $Mo_2C$ is 0.45 eV closer to the Fermi level than that of $Mo_2C$:1Fe. Thus, Mo in $Mo_2C$:1Fe will bind with H* weaker than that in pristine $Mo_2C$ and have a better HER catalytic activity. Besides *H adsorption strength, water dissociation is also an important step for HER activity under alkaline conditions. Our computational results indicate that the water dissociation step is an exothermic reaction for both $Mo_2C$ and $Mo_2C$:1Fe, while they are more energetically favorable on $Mo_2C$:1Fe as shown in Fig. S21.† Considering *H adsorption and water dissociation, we can conclude that Fe doping is an effective approach to enhance the HER activity under alkaline conditions. This result reinforces the presence of the synergy between $Mo_2C$ and Fe dopants, providing outstanding catalytic activity to the Mo–Mo bridge site in $Mo_2C$ and making 0.5% Fe-$Mo_2C$@NCF a highly efficient HER catalyst.

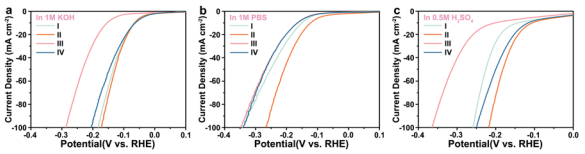


Fig. 5 The iR-corrected polarization curves at a scan rate of 5 mV $s^{-1}$ of (I) 0.5% Mn-$Mo_2C$@NCF, (II) 0.5% Fe-$Mo_2C$@NCF, (III) 0.5% Co-$Mo_2C$@NCF, and (IV) 0.5% Ni-$Mo_2C$@NCF electrocatalysts in 1.0 M KOH (a), 1.0 M PBS (b), and 0.5 M $H_2SO_4$ (c).

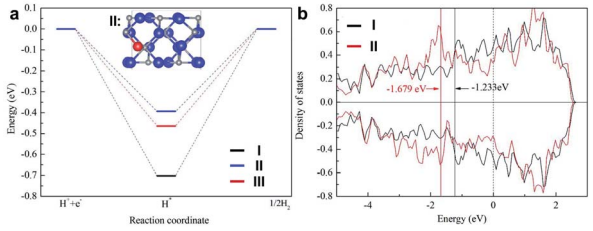


Fig. 6 (a) Free energy diagrams of the HER on pristine $Mo_2C$ (I), 0.5% Fe-$Mo_2C$ (II) and 1% Fe-$Mo_2C$ (III). (b) Partial density of states of the Mo-3d states at the adsorption sites on pristine $Mo_2C$ (I) and 0.5% Fe-$Mo_2C$ (II). The d-band center of each material is labelled with corresponding values.

## 4. Conclusions

In conclusion, Fe-doped molybdenum carbide on a nitrogen-doped carbon substrate (Fe-$Mo_2C$@NCF) with a loosely linked and channel-rich structure was prepared and proven to be a highly efficient electrocatalyst for the hydrogen evolution reaction over a wide pH range. Benefitting from the exposure of abundant active sites and excellent structural stability, the Fe-$Mo_2C$@NCF exhibits enhanced activity for the HER, such as a low $\eta_{10}$ of 65, 130 and 129 mV as well as $\eta_{100}$ of 172, 275 and 242 mV $dec^{-1}$ in 1.0 M KOH, 1.0 M PBS and 0.5 M $H_2SO_4$, respectively. In addition, the synergistic catalytic effects between the N-doped carbon substrate and Fe-doped $Mo_2C$ nanoparticles were realised, which can boost the continuous electron transport between metal dopants and transition metal carbide, optimise active species and enhance the corrosion resistance and stability of the catalyst.

## Conflicts of interest

There is no conflicts of interest.

## Acknowledgements

This work was supported the National Natural Science Foundation of China (No. 51873198, 51503184 and 21703248), the Strategic Priority Research Program of the Chinese Academy of Sciences (Grant No. XDB20000000), the Engineering and Physical Sciences Research Council (EPSRC, EP/R023581/1) and the STFC Batteries Network (ST/R006873/1).

## References

1 H. B. Wu, B. Y. Xia, L. Yu, X. Y. Yu and X. W. Lou, *Nat. Commun.*, 2015, **6**, 6512.

 

2 J. Zhang, T. Wang, P. Liu, Z. Liao, S. Liu, X. Zhuang, M. Chen, E. Zschech and X. Feng, *Nat. Commun.*, 2017, **8**, 15437.
3 M. Hou, X. Teng, J. Wang, Y. Liu, L. Guo, L. Ji, C. Cheng and Z. Chen, *Nanoscale*, 2018, **10**, 14594–14599.
4 Y. Li, H. Wang, L. Xie, Y. Liang, G. Hong and H. Dai, *J. Am. Chem. Soc.*, 2011, **133**, 7296–7299.
5 D. Voiry, H. Yamaguchi, J. Li, R. Silva, D. C. Alves, T. Fujita, M. Chen, T. Asefa, V. B. Shenoy, G. Eda and M. Chhowalla, *Nat. Mater.*, 2013, **12**, 850–855.
6 E. J. Popczun, J. R. McKone, C. G. Read, A. J. Biacchi, A. M. Wiltrout, N. S. Lewis and R. E. Schaak, *J. Am. Chem. Soc.*, 2013, **135**, 9267–9270.
7 D. Voiry, H. S. Shin, K. P. Loh and M. Chhowalla, *Nat. Rev. Chem.*, 2018, **2**, 0105.
8 M. Y. Zu, P. F. Liu, C. Wang, Y. Wang, L. R. Zheng, B. Zhang, H. Zhao and H. G. Yang, *ACS Energy Lett.*, 2017, **3**, 78–84.
9 G. Zhao, K. Rui, S. X. Dou and W. Sun, *Adv. Funct. Mater.*, 2018, **28**, 1803291.
10 J. Yu, Q. He, G. Yang, W. Zhou, Z. Shao and M. Ni, *ACS Catal.*, 2019, **9**, 9973–10011.
11 S.-Y. Bae, J. Mahmood, I.-Y. Jeon and J.-B. Baek, *Nanoscale Horiz.*, 2020, **5**, 43–56.
12 J. Tian, Q. Liu, A. M. Asiri and X. Sun, *J. Am. Chem. Soc.*, 2014, **136**, 7587–7590.
13 Y. Zheng, Y. Jiao, M. Jaroniec and S. Z. Qiao, *Angew. Chem., Int. Ed.*, 2015, **127**, 52–66.
14 Z. Pu, M. Wang, Z. Kou, I. S. Amiinu and S. Mu, *Chem. Commun.*, 2016, **52**, 12753–12756.
15 S. Wang, L. Pan, J. J. Song, W. Mi, J. J. Zou, L. Wang and X. Zhang, *J. Am. Chem. Soc.*, 2015, **137**, 2975–2983.
16 Y. Huang, H. Lu, H. Gu, J. Fu, S. Mo, C. Wei, Y. E. Miao and T. Liu, *Nanoscale*, 2015, **7**, 18595–18602.
17 W.-F. Chen, S. Iyer, S. Iyer, K. Sasaki, C.-H. Wang, Y. Zhu, J. T. Muckerman and E. Fujita, *Energy Environ. Sci.*, 2013, **6**, 1818.
18 J. G. Chen, *Chem. Rev.*, 1996, **96**, 1477–1498.
19 R. Michalsky, Y.-J. Zhang and A. A. Peterson, *ACS Catal.*, 2014, **4**, 1274–1278.
20 S. Park, J. Park, H. Abroshan, L. Zhang, J. K. Kim, J. Zhang, J. Guo, S. Siahrostami and X. Zheng, *ACS Energy Lett.*, 2018, **3**, 2685–2693.
21 J. Deng, H. Li, S. Wang, D. Ding, M. Chen, C. Liu, Z. Tian, K. S. Novoselov, C. Ma, D. Deng and X. Bao, *Nat. Commun.*, 2017, **8**, 14430.
22 K. Ojha, S. Saha, S. Banerjee and A. K. Ganguli, *ACS Appl. Mater. Interfaces*, 2017, **9**, 19455–19461.
23 H. Wang, L. Ouyang, G. Zou, C. Sun, J. Hu, X. Xiao and L. Gao, *ACS Catal.*, 2018, **8**, 9529–9536.
24 S. Zhao, J. Berry-Gair, W. Li, G. Guan, M. Yang, J. Li, F. Lai, F. Corà, K. Holt, D. J. L. Brett, G. He and I. P. Parkin, *Adv. Sci.*, 2020, 1903674.
25 H. Yan, Y. Xie, Y. Jiao, A. Wu, C. Tian, X. Zhang, L. Wang and H. Fu, *Adv. Mater.*, 2018, **30**, 1704156.
26 R. Kumar, R. Rai, S. Gautam, A. De Sarkar, N. Tiwari, S. N. Jha, D. Bhattacharyya, A. K. Ganguli and V. Bagchi, *J. Mater. Chem. A*, 2017, **5**, 7764–7768.
27 W. F. Chen, K. Sasaki, C. Ma, A. I. Frenkel, N. Marinkovic, J. T. Muckerman, Y. Zhu and R. R. Adzic, *Angew. Chem., Int. Ed.*, 2012, **51**, 6131–6135.
28 J. Yang, F. Zhang, X. Wang, D. He, G. Wu, Q. Yang, X. Hong, Y. Wu and Y. Li, *Angew. Chem., Int. Ed.*, 2016, **55**, 12854–12858.
29 T. Wang, K. Du, W. Liu, Z. Zhu, Y. Shao and M. Li, *J. Mater. Chem. A*, 2015, **3**, 4368–4373.
30 L. Yu, I. K. Mishra, Y. Xie, H. Zhou, J. Sun, J. Zhou, Y. Ni, D. Luo, F. Yu, Y. Yu, S. Chen and Z. Ren, *Nano Energy*, 2018, **53**, 492–500.
31 Y. Huang, Q. Gong, X. Song, K. Feng, K. Nie, F. Zhao, Y. Wang, M. Zeng, J. Zhong and Y. Li, *ACS Nano*, 2016, **10**, 11337–11343.
32 J. Xiong, J. Li, J. Shi, X. Zhang, N.-T. Suen, Z. Liu, Y. Huang, G. Xu, W. Cai, X. Lei, L. Feng, Z. Yang, L. Huang and H. Cheng, *ACS Energy Lett.*, 2018, **3**, 341–348.
33 J. Wan, J. Wu, X. Gao, T. Li, Z. Hu, H. Yu and L. Huang, *Adv. Funct. Mater.*, 2017, **27**, 1703933.
34 H. Sun, Y. Lian, C. Yang, L. Xiong, P. Qi, Q. Mu, X. Zhao, J. Guo, Z. Deng and Y. Peng, *Energy Environ. Sci.*, 2018, **11**, 2363–2371.
35 Y. Zhang, B. Ouyang, J. Xu, S. Chen, R. S. Rawat and H. J. Fan, *Adv. Energy Mater.*, 2016, **6**, 1600221.
36 H. Vrubel and X. Hu, *Angew. Chem., Int. Ed.*, 2012, **51**, 12703–12706.
37 P. Xiao, X. Ge, H. Wang, Z. Liu, A. Fisher and X. Wang, *Adv. Funct. Mater.*, 2015, **25**, 1520–1526.
38 W. F. Chen, C. H. Wang, K. Sasaki, N. Marinkovic, W. Xu, J. T. Muckerman, Y. Zhu and R. R. Adzic, *Energy Environ. Sci.*, 2013, **6**, 943.
39 Y. Shi and B. Zhang, *Chem. Soc. Rev.*, 2016, **45**, 1781.
40 J. Greeley, T. F. Jaramillo, J. Bonde, I. B. Chorkendorff and J. K. Norskov, *Nat. Mater.*, 2006, **5**, 909–913.
41 Q. Gao, W. Zhang, Z. Shi, L. Yang and Y. Tang, *Adv. Mater.*, 2019, **31**, e1802880.
42 Y. Ma, G. Guan, X. Hao, J. Cao and A. Abudula, *Renewable Sustainable Energy Rev.*, 2017, **75**, 1101–1129.
43 J. Yin, Q. Fan, Y. Li, F. Cheng, P. Zhou, P. Xi and S. Sun, *J. Am. Chem. Soc.*, 2016, **138**, 14546–14549.
44 S. Jing, L. Zhang, L. Luo, J. Lu, S. Yin, P. K. Shen and P. Tsiakaras, *Appl. Catal., B*, 2018, **224**, 533–540.
45 K. Lan, L. Gong, M. Yang, X. Huang, P. Jiang, K. Wang, L. Ma and R. Li, *J. Colloid Interface Sci.*, 2019, **553**, 148–155.
46 Y. Ma, M. Chen, H. Geng, H. Dong, P. Wu, X. Li, G. Guan and T. Wang, *Adv. Funct. Mater.*, 2020, **30**, 2000561.
47 C. Wan and B. M. Leonard, *Chem. Mater.*, 2015, **27**, 4281–4288.
48 J. S. Li, Y. Wang, C. H. Liu, S. L. Li, Y. G. Wang, L. Z. Dong, Z. H. Dai, Y. F. Li and Y. Q. Lan, *Nat. Commun.*, 2016, **7**, 11204.
49 K. Xiong, L. Li, L. Zhang, W. Ding, L. Peng, Y. Wang, S. Chen, S. Tan and Z. Wei, *J. Mater. Chem. A*, 2015, **3**, 1863–1867.
50 H. Lin, Z. Shi, S. He, X. Yu, S. Wang, Q. Gao and Y. Tang, *Chem. Sci.*, 2016, **7**, 3399–3405.
51 H. Lin, N. Liu, Z. Shi, Y. Guo, Y. Tang and Q. Gao, *Adv. Funct. Mater.*, 2016, **26**, 5590–5598.

52 Z.-Y. Wu, B.-C. Hu, P. Wu, H.-W. Liang, Z.-L. Yu, Y. Lin, Y.-R. Zheng, Z. Li and S.-H. Yu, *NPG Asia Mater.*, 2016, **8**, e288.
53 H. Ang, H. Wang, B. Li, Y. Zong, X. Wang and Q. Yan, *Small*, 2016, **12**, 2859–2865.
54 Y. Liu, G. Yu, G. D. Li, Y. Sun, T. Asefa, W. Chen and X. Zou, *Angew. Chem., Int. Ed.*, 2015, **54**, 10752–10757.
55 C. Wan, Y. N. Regmi and B. M. Leonard, *Angew. Chem., Int. Ed.*, 2014, **53**, 6407–6410.
56 R. Ma, Y. Zhou, Y. Chen, P. Li, Q. Liu and J. Wang, *Angew. Chem., Int. Ed.*, 2015, **54**, 14723–14727.
57 W. F. Chen, K. Sasaki, C. Ma, A. I. Frenkel, N. Marinkovic, J. T. Muckerman, Y. Zhu and R. R. Adzic, *Angew. Chem., Int. Ed.*, 2012, **51**, 6131–6135.
58 J. Duan, S. Chen, M. Jaroniec and S. Z. Qiao, *ACS Nano*, 2015, **9**, 931–940.
59 L. Lai, J. R. Potts, D. Zhan, L. Wang, C. K. Poh, C. Tang, H. Gong, Z. Shen, J. Lin and R. S. Ruoff, *Energy Environ. Sci.*, 2012, **5**, 7936.
60 Q. Liu, J. Tian, W. Cui, P. Jiang, N. Cheng, A. M. Asiri and X. Sun, *Angew. Chem., Int. Ed.*, 2014, **53**, 6710–6714.
61 C. He and J. Tao, *Chem. Commun.*, 2015, **51**, 8323–8325.
62 B. Hinnemann, P. G. Moses, J. Bonde, K. P. Jørgensen, J. H. Nielsen, S. Horch, I. Chorkendorff and J. K. Nørskov, *J. Am. Chem. Soc.*, 2005, **127**, 5308–5309.
63 A. Le Goff, V. Artero, B. Jousselme, P. D. Tran, N. Guillet, R. Métayé, A. Fihri, S. Palacin and M. Fontecave, *Science*, 2009, **326**, 1384–1387.
64 A. Kundu, J. N. Sahu, G. Redzwan and M. Hashim, *Int. J. Hydrogen Energy*, 2013, **38**, 1745–1757.
65 R. LeRoy, *Int. J. Hydrogen Energy*, 1983, **8**, 401–417.
66 S. T. Oyama, T. Gott, H. Zhao and Y.-K. Lee, *Catal. Today*, 2009, **143**, 94–107.
67 S. Carenco, D. Portehault, C. Boissiere, N. Mezailles and C. Sanchez, *Chem. Rev.*, 2013, **113**, 7981–8065.
68 H. Lin, N. Liu, Z. Shi, Y. Guo, Y. Tang and Q. Gao, *Adv. Funct. Mater.*, 2016, **26**, 5590–5598.
69 J. Tian, Q. Liu, N. Cheng, A. M. Asiri and X. Sun, *Angew. Chem., Int. Ed.*, 2014, **53**, 9577–9581.
70 Z. Lu, L. Qian, Y. Tian, Y. Li, X. Sun and X. Duan, *Chem. Commun.*, 2016, **52**, 908–911.